Mathematics and Computers in Simulation 228 (2025) 87–102

Contents lists available at ScienceDirect

Mathematics and Computers in Simulation

journal homepage: www.elsevier.com/locate/matcom

Original articles

Modeling low-intensity ultrasound mechanotherapy impact on growing cancer stem cells

Beatriz Blanco [a,b,c], Roberto Palma [d], Manuel Hurtado [b,c,d], Gema Jiménez [b,c,e], Carmen Griñán-Lisón [b,c,e], Juan Melchor [b,c,f], Juan Antonio Marchal [b,c,e], Hector Gomez [g,h,i], Guillermo Rus [b,c,d], Juan Soler [a,c,*]

[a] Department of Applied Mathematics, University of Granada, Granada, 18001, Spain
[b] Instituto de Investigación Biosanitaria, ibs.GRANADA, 18012 Granada, Spain
[c] Research Unit "Modelling Nature" (MNat), University of Granada, Granada 18001, Spain
[d] Department of Structural Mechanics, University of Granada, Granada, 18001, Spain
[e] Department of Human Anatomy and Embryology, University of Granada, Granada, 18001, Spain
[f] Department of Statistics and Operations Research, University of Granada, Granada, 18001, Spain
[g] School of Mechanical Engineering, Purdue University, West Lafayette, IN, 47907, United States of America
[h] Weldon School of Biomedical Engineering, Purdue University, West Lafayette, IN, 47907, United States of America
[i] Purdue Center for Cancer Research, Purdue University, West Lafayette, IN, 47907, United States of America

ARTICLE INFO

Keywords:
Cancer stem cells
Computational mechanics
Low-intensity ultrasound
Mechanotherapy
Multiscale modeling
Tumor forecasting

ABSTRACT

Targeted therapeutic interventions utilizing low-intensity ultrasound (LIUS) exhibit substantial potential for hindering the proliferation of cancer stem cells. This investigation introduces a multiscale model and computational framework to comprehensively explore the therapeutic LIUS on poroelastic tumor dynamics, thereby unraveling the intricacies of mechanotransduction mechanisms at play. Our model includes both macroscopic timescales encompassing days and rapid timescales spanning from microseconds to seconds, facilitating an in-depth comprehension of tumor behavior. We unveil the discerning suppression or reorientation of cancer cell proliferation and migration, enhancing a notable redistribution of cellular phases and stresses within the tumor microenvironment. Our findings defy existing paradigms by elucidating the impact of LIUS on cancer stem cell behavior. This endeavor advances our fundamental understanding of mechanotransduction phenomena in the context of LIUS therapy, thus underscoring its promising as a targeted therapeutic modality for cancer treatment. Furthermore, our results make a substantial contribution to the broader scientific community by shedding light on the intricate interplay between mechanical forces, cellular responses, and the spatiotemporal evolution of tumors. These insights hold the promising to promote a new perspective for the future development of pioneering and highly efficacious therapeutic strategies for combating cancer in a personalized manner.

1. Introduction

Mechanotherapy represents an emerging frontier in cancer treatment, harnessing the power of mechanical forces *per se*, or through their interaction with cell biochemical connections, to selectively target and eradicate or reverse the growth trend of cancer

* Corresponding author.
E-mail address: jsoler@ugr.es (J. Soler).

https://doi.org/10.1016/j.matcom.2024.08.030
Received 28 January 2024; Received in revised form 16 June 2024; Accepted 25 August 2024
Available online 4 September 2024

cells. The underlying principle behind this strategy lies in the observation that cancer cells exhibit increased sensitivity to mechanical stimuli, and by manipulating these forces, their properties can be affected, ultimately leading to cell death or dysfunction.

In the past few years, extensive endeavors have been dedicated to develop a wide range of techniques aimed at modulating cell behavior by altering the microenvironment. These techniques encompass a spectrum of perspectives, from pharmacological agents that modify the elasticity of the remodeled microenvironment and cell stiffness [1–5], to the application of mechanical waves. These principles not only serve as fundamental research tools for investigating the basic interactions of cell mechanics, but an extraordinary translational potential could also emerge for clinical applications, since mechanical waves can be delivered to patients using transducers or patches. In addition, there is growing recognition that the combination of these therapies can synergistically enhance treatment effectiveness and greatly improve the overall prognosis of the disease.

Recent studies have provided compelling evidence of the therapeutic effectiveness of low-intensity ultrasound. Low-intensity ultrasound (LIUS) and its pulsed version (LIPUS), have been proposed to impact cancer cells by two main mechanisms: (i) selectively resonating the right diameter cells under the name of *oncotripsy*, which lies on destroying the cytoskeleton via cavitation [6–11], and (ii) triggered response produced via mechanotransduction signaling pathways [9,10,12–21].

Although these studies have repeatedly evidenced considerable promising effects, the lack of understanding of the mechanism, and the even opposing responses triggered by diverse frequencies, energies, and configurations, make the concept of little use at its current state.

The deepening in the configuration and effects of the application of mechanical waves have garnered considerable attention in the scientific community, driven by the potential of LIUS to influence cancer cell dynamics. However, our understanding of the underlying mechanisms behind LIUS-induced effects in cancer cells has been hampered by the complexity of accounting for the combined effects of the large number of agents involved in this process, and the enormous costs associated with performing extensive biological experiments.

To unravel the intricate mechanisms of LIUS and improve its therapeutic prospective, mathematical oncology emerges as a valuable tool [22]. By simulating the complex interactions between ultrasound waves and the tumor microenvironment, in conjunction with other treatment modalities, these models offer a great avenue to try to understand LIUS at a deeper level. Such ultrasound-tumor interactions provide crucial insights into the underlying mechanisms of LIUS and can facilitate the development of more efficient treatment strategies.

Within this framework, we present a multiscale model to unveil the influence of LIUS on tumor evolution through mechanotransduction. Our approach encompasses the application of LIUS at high frequencies coupled with lower acoustic pressures to target cancer precursor cells known as cancer stem cells (CSCs) [23,24], which are widely considered to have an important impact on cancer metastasis and are frequently associated with relapse due to their self-renewal, differentiation capabilities and resistance to conventional therapies [24].

The structure of the article is organized as follows: Section 2 outlines a multiscale mathematical model that conceptualizes tumors as poroelastic materials, comprising an interstitial fluid phase and distinct solid phases that are influenced by the elastic properties of tumor cells, healthy cells, and the extracellular matrix (ECM). We have expanded upon an existing framework [25,26], incorporating the impact of ultrasound on this system and introducing a novel mechanotransduction function that is sensitive to hydrostatic stress. Subsequently, we explore the results, which are methodically divided into two sections. In the initial results Section 3.1, we apply the mathematical model in a simplified context—focusing solely on the presence of tumor cells—and present both experimental and numerical outcomes from our investigations with CSCs. By varying frequencies, viscosities, and acoustic pressures, we illustrate how LIUS influences CSCs compared to unsonicated CSCs over a period of three days. In the subsequent Section 3.2, armed with the previously refined mechanical and mechanotransduction parameters, we employ the complete mathematical model to predict the effects of ultrasound in scenarios where various cellular types coexist. Here, we identify the selective patterns of LIUS and we reproduce and elucidate the selective behavior of LIUS when targeting cancerous cells. Finally, in Section 4, we discuss the significant findings of this research, highlighting how our interdisciplinary approach offers a promising avenue for exploring the therapeutic effects of LIUS on cancer stem cells.

2. Materials and methods

2.1. Mathematical model

The multiscale model is proposed on two different scales: (i) slow time scale, t, in which the tumor grows and migrates, and (ii) fast time scale, t_u, in which ultrasound propagates through the tumor. Both scales are coupled by mechanotransduction, which occurs at an ultrasonic time interval and triggers a tumor dynamics response at a slow scale. Thus, we can encapsulate the enduring effects of growth and reorganization, which may not be discernible on the ultrasonic scale but acquire significance on a broader and slower scale [27].

We describe tumors as poroelastic materials composed of a fluid phase (ϕ_F) of interstitial fluid and different solid phases (ϕ_i) that provide elastic stiffness. The solid phases included here are tumor cells (ϕ_T), healthy cells (ϕ_H), and the extracellular matrix (ϕ_M). This study simplifies the representation of the tumor environment by treating these cell types and the ECM phase generically, despite the significant inherent differences between them. For instance, the ECM is considered as a uniform composite of fibrous tissue, proteins and other components, although it actually comprises various types with distinct roles. Similarly, the model does not distinguish between the nuanced behaviors of endothelial versus immune and normal epithelial cells, especially concerning their

competitive interactions within the tumor microenvironment. This approach allows for a more general analysis but overlooks the complex heterogeneity typical of such biological systems.

The proposed system is built upon Biot's poroelasticity and growth theory, widely studied in the field of thermodynamics. For a comprehensive grasp of the equations, particularly those pertaining to poroelastic cell competition and mechanotransduction, we suggest consulting Refs. [20,25,26,28]. We consider infinitesimal strain theory and linear elasticity assuming that there is no large deformation during ultrasound insonation [6] and growth does not develop great deformation. Furthermore, we use the $\boldsymbol{u}-p$ poroelastic notation, neglecting the relative fluid-solid displacement.

The momentum balance that describes the dynamic mechanical equilibrium is:

$$\nabla \cdot \boldsymbol{\sigma} = \rho \frac{\partial^2 \mathbf{u}}{\partial t^2}, \tag{1}$$

where ρ is the medium density and $\mathbf{u}$ are the displacements. The multiscale Cauchy stress tensor in a sonicated growing tumor is described by:

$$\boldsymbol{\sigma}(\boldsymbol{x}, t) = \boldsymbol{\sigma}_s(\boldsymbol{x}, t) + \boldsymbol{\sigma}_u(\boldsymbol{x}, t_u), \tag{2}$$

where the slow-scale stress $\boldsymbol{\sigma}_s(\boldsymbol{x}, t)$ accounts for the growth and the poroelastic rearrangements while the fast-scale stress $\boldsymbol{\sigma}_u(\boldsymbol{x}, t_u)$ is the ultrasonic stress. To isolate the governing equations at each temporal scale and save computational cost, we follow the principles of multiscale developed in [29] and adapted to the ultrasound formulation in [27]. Then, we define the average of the multiscale stress over an ultrasonic spatial and temporal cycle, specifically, the reference ultrasonic wavelength λ and period T:

$$\langle \boldsymbol{\sigma} \rangle = \frac{1}{\lambda T} \int_0^T \int_0^\lambda \boldsymbol{\sigma} \, d\boldsymbol{x} \, dt_u. \tag{3}$$

Considering the definition of multiscale stress, the above reads:

$$\langle \boldsymbol{\sigma} \rangle = \frac{1}{\lambda T} \int_0^T \int_0^\lambda \boldsymbol{\sigma}_s \, d\boldsymbol{x} \, dt_u + \frac{1}{\lambda T} \int_0^T \int_0^\lambda \boldsymbol{\sigma}_u \, d\boldsymbol{x} \, dt_u, \tag{4}$$

where the slow stress independent of the ultrasonic scale is $\langle \boldsymbol{\sigma}_s \rangle = \boldsymbol{\sigma}_s$. Ultrasonic stress is a sinus function on λ and T, so $\langle \boldsymbol{\sigma}_u \rangle = 0$. Then, the average of the multiscale stress is the slow-scale stress, $\langle \boldsymbol{\sigma} \rangle = \boldsymbol{\sigma}_s$, and subsequently the average of the slow-scale stress is the total multiscale stress, $\langle \boldsymbol{\sigma}_s \rangle = \boldsymbol{\sigma}$. Finally, with respect to Eq. (2) and the independence of the slow-scale stress from the ultrasonic scale, the ultrasonic stress is $\boldsymbol{\sigma}_u = \boldsymbol{\sigma} - \langle \boldsymbol{\sigma} \rangle$.

Once the multiscale approach is formalized, we define the slow-scale stress as an additive decomposition:

$$\boldsymbol{\sigma}_s = \boldsymbol{\sigma}_e + \boldsymbol{\sigma}_p + \boldsymbol{\sigma}_g, \tag{5}$$

where $\boldsymbol{\sigma}_{\mathrm{e}}$ is the so-called effective solid stress tensor, $\boldsymbol{\sigma}_{\mathrm{p}}$ the fluid pressure contribution, and $\boldsymbol{\sigma}_{\mathrm{g}}$ the stress generated during growth. Hence, the equation of equilibrium (1) applied to slow-scale stress can be considered as a quasistatic process since characteristic velocities are small and inertia terms can be neglected [30]. For an elastic isotropic material, the constitutive equation for the effective solid stress that accounts for the elastic rearrangements yields:

$$\boldsymbol{\sigma}_e = 2\mu_d \left(\boldsymbol{\varepsilon} - \frac{1}{3} \mathrm{tr}(\boldsymbol{\varepsilon}) \mathbf{I} \right) + K_d \mathrm{tr}(\boldsymbol{\varepsilon}) \mathbf{I}, \tag{6}$$

where the small strain is $\varepsilon = \frac{1}{2}(\nabla \mathbf{u} + \nabla \mathbf{u}^{\mathrm{T}})$, with $\mathbf{u}$ the displacements, $\mathbf{I}$ the second-order identity tensor, and K_d and μ_d the drained bulk and shear modulus. We can neglect the viscous solid contribution in the slow-scale governing equation since the relaxation terms of rearrangements are on a smaller time scale than growth. The stress produced by the fluid is:

$$\boldsymbol{\sigma}_p = -\alpha \left(p - p_0 \right) \mathbf{I}, \tag{7}$$

with α the Biot coefficient, p the fluid pore pressure, and p_0 the initial fluid pore pressure. The evolution of the fluid pressure p is regulated by the storage equation:

$$\frac{\partial \zeta}{\partial t} = \frac{1}{M} \frac{\partial p}{\partial t} + \alpha \frac{\partial tr(\boldsymbol{\varepsilon})}{\partial t} = \nabla \cdot \left(k \nabla p \right) + \Gamma_{\mathrm{F}}, \tag{8}$$

where ζ is the dimensionless variation of fluid content defined by the difference between the actual and initial fluid phase $\zeta = \phi_{\mathrm{F}} - \phi_{\mathrm{F0}}$. The parameter M represents the Biot modulus, and k denotes the hydraulic conductivity, given by $k = \kappa {\nu_f}^{-1}$, where κ stands for the permeability of the medium, and the dynamic fluid viscosity is described by ν_f. The source term Γ_F accounts for the fluid interchange between vessels and capillaries. Considering the theory of Starling [25,26,31–33], the fluid flow source yields:

$$\Gamma_F = k_v \left[(p_v - p) - \omega(\pi_v - \pi_l) \right] - k_l (p - p_l), \tag{9}$$

where p_v is associated with the vessel pressure, ω represents the reflection coefficient, weighing the interstitial osmotic pressure $(\pi_v - \pi_l)$, and p_l denotes the lymphatic pressure drainage operating counter to the vessel pressure system. The constants k_v and k_l correspond to the conductivity coefficients of the vessel and lymphatic system, respectively. Following recent literature, we formulate the conductivity of the lymphatic system as a function of tumor cells, encompassing the diminishing drainage of the lymphatic system induced by tumor growth.

$$k_l = \left[1 - (\phi_T - \phi_{T0}) \right] k_{ln}, \tag{10}$$

where k_{ln} is the conductivity of the lymphatic system under normal conditions [26,31]. Finally, the stress produced by growth reads:

$$\boldsymbol{\sigma}_g = -Kg\boldsymbol{\gamma}, \tag{11}$$

where g is the growth strain function and $\boldsymbol{\gamma}$ is the tensor that distributes the growth in different directions. In this study, we have assumed isotropic growth, so $\boldsymbol{\gamma} = \frac{1}{3}\mathbf{I}$. The growth function is considered homogeneous and, therefore, can be written as:

$$g = \phi_T + \phi_H + \phi_M - \phi_{T0} - \phi_{H0} - \phi_{M0}, \tag{12}$$

with the zero subindexes denoting the initial volume fractions. The volumetric fractions evolve and interact with the mechanical environment and are governed by:

$$\begin{aligned}
\frac{\partial \phi_T}{\partial t} &= \nabla \cdot \left(\mathcal{M}_T D_T \phi_T \nabla \phi_T\right) + \phi_{\mathrm{F}} \mathcal{M}_{\mathrm{T}} \phi_{\mathrm{T}} \Gamma_{\mathrm{T}} \mathrm{T}_{\mathrm{T}}, \\
\frac{\partial \phi_H}{\partial t} &= \phi_F \mathcal{M}_H \phi_H \Gamma_H T_H, \\
\frac{\partial \phi_M}{\partial t} &= \beta_T \phi_T + \beta_H \phi_H - \delta_M \phi_M \Gamma_M,
\end{aligned} \tag{13}$$

where the first equation describes the tumor cell dynamics. In particular, the first term on the right hand side accounts for tumor non-linear cell flux, described here by a finite speed tumor propagation front limited by the diffusion coefficient D_T, although a controlled velocity of propagation could be also taken into account [20,34–37]. The second term considers the competitive interaction among other species – Γ_{T} –, and both terms account for the mechanotransduction function – $\mathcal{M}_{\mathrm{T}}$ –. It should be highlighted that the role of mechanotransduction is conceptually unified for both the migration and proliferative terms, echoing conclusions drawn in prior research [30]. Nonetheless, a more sophisticated model could differentiate between these phases by delineating specific signaling pathway and associated proteins [20], thereby assigning unique pathways and precise functions to each phase distinctly.

Mechanotransduction and competition are also described for healthy cells by $\mathcal{M}_{\mathrm{H}}$ and Γ_{H}. The proliferation rates are defined by T_{T} and T_{H} for tumor and healthy cells respectively. The ECM evolution depends on the species interaction Γ_{M} and on the ECM synthesis promoted by the cells by the production rates β_T and β_H, and the ECM degradation processes enabled by the loss rate δ_M [26]. The competition terms Γ_T, Γ_H and Γ_M are defined by the following Volterra-Lotka dynamics, see [26]:

$$\begin{aligned}
\Gamma_T &= \left(1 - \alpha_{TT}\phi_T - \alpha_{TH}\phi_H - \alpha_{TM}\phi_M\right), \\
\Gamma_H &= \left(1 - \alpha_{HT}\phi_T - \alpha_{HH}\phi_H - \alpha_{HM}\phi_M\right), \\
\Gamma_M &= \alpha_{MT}\phi_T + \alpha_{MH}\phi_H,
\end{aligned} \tag{14}$$

where the coefficients α_{ij}, with $i, j = \{T, H, M\}$, represent the interaction among the cell species. To complete the system of equations, we define the mechanotransduction function based on previously validated expressions [20]. Thus, the function of mechanotransduction is defined in an ultrasonic time period in which cell mechanosensors could receive signaling linked to the cytoskeleton network extremely quickly [17,38], and then respond triggering changes in proliferation and migration, as proposed in [18,38]. Then, we propose that cells perceive the average of the sigmoid function $\mathcal{M}_{B_i}$ at an ultrasonic time interval, in which cells could sense perturbations and activate mechanotransduction pathways that alter proliferation above a certain stress threshold [19,21] – see Fig. 1 –. Then, mechanotransduction can be expressed as:

$$\mathcal{M}_i = \frac{1}{T}\int_0^T \mathcal{M}_{B_i}\, dt_u, \tag{15}$$

where the subscript i refers to tumor or healthy cells, and $\mathcal{M}_{B_i}$ is based on [26]:

$$\mathcal{M}_{B_i} = \left[q_i + (1 - q_i)e^{b_i(|\sigma_{\mathcal{M}}| - \beta_u \sigma_{L_i})}\right] \left(1 + e^{b_i(|\sigma_{\mathcal{M}}| - \beta_u \sigma_{L_i})}\right)^{-1}. \tag{16}$$

Indeed, the initial proliferation or migration of cells decreases to the maximum of the viability of the cells, achieving the factor of q_i when the stress perceived by the cells $\sigma_{\mathcal{M}}$ in the environment exceeds a threshold σ_{L_i}. In the literature, this threshold is obtained for static stress and values between [1–10] kPa [25,26,32,39–41]. However, to also account for dynamic stress, we adopt a linear parameter β_u, which reduces the sensitivity limit of cells. This hypothesis is rooted in the understanding that static stress necessitates higher intensity to elicit a response due to stress dissipation, while dynamic pressure operates within a compressed time frame, precluding dissipation. Key factors influencing dissipation include the cytoskeleton, which imparts structural integrity to cells and facilitates the redistribution of mechanical loads within them, as well as the viscosity of solid phases and the dissipation of stresses through interstitial fluid perfusion via pores. The parameter b_i refers to the smoothness of the transition zone of the sigmoid function and determines how fast or slow cells adapt their proliferation to stress.

Then, cells detect both static hydrostatic growth-induced stress and dynamic ultrasonic-induced stress through mechanotransduction pathways and the total stress perceived yields:

$$\sigma_{\mathcal{M}} = \sigma_s^h + \sigma_u^h, \tag{17}$$

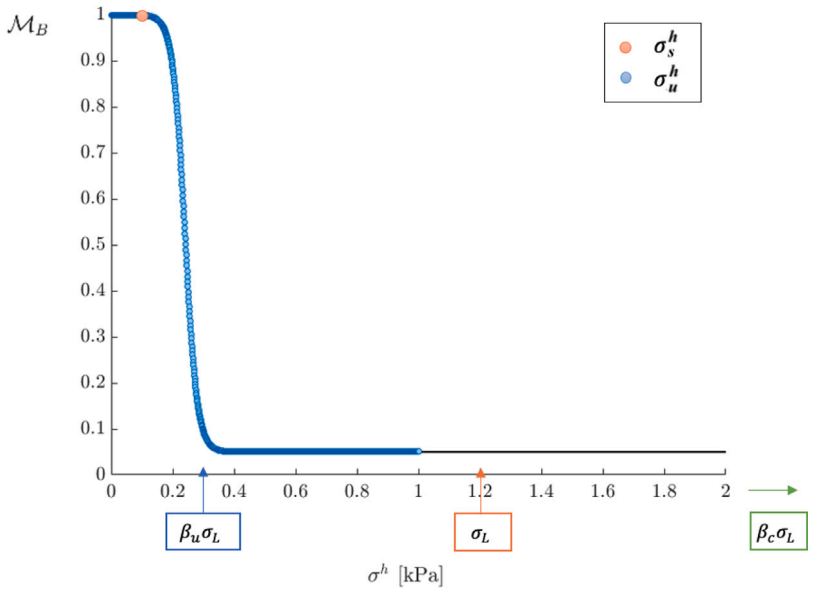

Fig. 1. Mechanotransduction function in an ultrasonic interval. Cells perceive the average of the sigmoid function $\mathcal{M}_B$. The slow ultrasound stress is constant at an ultrasonic time interval, while ultrasound stress exhibits dynamic behavior, oscillating between rarefaction and compression – for this case, we have plotted the absolute stress of a wave with an amplitude of 1 kPa –. To account for the dynamic nature of ultrasound stress, the static stress limit σ_L is decreased by a coefficient β_u. However, if the limit is exceeded – this limit could be named β_c instead of β_u – it may result in cell disruption and cessation of proliferation or migration, indicated by $\mathcal{M}_B = 0$.

where the superscript h denotes the hydrostatic stress defined by $\sigma^h = \frac{1}{3}\mathrm{tr}(\boldsymbol{\sigma})$ for each time-scale stress. Shear stress contribution is disregarded in our analysis due to the plane ultrasound wave and isotropic growth, as its magnitude is three orders of magnitude smaller than that of the normal components.

We obtain $\boldsymbol{\sigma}_u$ over a period of time from the propagation of a P-wave emitted by a transducer through the medium. We formulate the displacement of the wave as a boundary condition, for instance, in a lateral face. Then, displacements generated by a transducer in the y-axis direction are described in the simplified form:

$$\mathbf{u}_u = \Big(0, A\sin(2\pi f t_u)\Big), \tag{18}$$

where A is the wave amplitude in terms of displacements and f is the central frequency. Before natural attenuation, the wave travels at speed $c_p = \sqrt{\frac{K+4/3\mu}{\rho}}$, where K and μ are the undrained bulk and shear modulus, and ρ stands for medium density.

The dynamic balance equation accounts for the inertial terms produced during sonication can be written as:

$$\nabla \cdot \boldsymbol{\sigma}_u = \rho \frac{\partial^2 \mathbf{u}_u}{\partial {t_u}^2}, \tag{19}$$

where $\boldsymbol{\sigma}_\mathrm{u}$ is the stress produced by mechanical wave propagation. To accurately represent the complex attenuation that occurs on a fast time scale, we utilize the Kelvin-Voigt governing equation as presented below:

$$\boldsymbol{\sigma}_u = 2\mu\Big(\boldsymbol{\varepsilon}_u - \frac{1}{3}\mathrm{tr}(\boldsymbol{\varepsilon}_u)\mathbf{I}\Big) + K\mathrm{tr}(\boldsymbol{\varepsilon}_u)\mathbf{I} + \eta_K \frac{\partial \mathrm{tr}(\boldsymbol{\varepsilon}_u)}{\partial t_u}\mathbf{I}, \tag{20}$$

where the small strain is $\boldsymbol{\varepsilon}_u = \frac{1}{2}(\nabla \mathbf{u}_u + \nabla \mathbf{u}_u{}^\mathrm{T})$. Attenuation is described by the volumetric viscosity η_K, neglecting the contribution of the shear viscosity due to the low order of magnitude of the shear component of the compression waves. As described in previous works [42,43], we define $\eta_K = \frac{\alpha_\eta 2\rho {c_p}^3}{(2\pi f)^2}$, considering the attenuation coefficient α_η of an ultrasonic wave at a given frequency [44].

2.2. Numerical methods

Regarding the initial conditions, the initial fluid phase is defined by the equation $\phi_{\mathrm{F0}} = 1 - \phi_{\mathrm{T0}} - \phi_{\mathrm{H0}} - \phi_{\mathrm{M0}}$. The initial fluid pressure guarantees the equilibrium of the storage equation, so p_0 causes the source term to be null at the initial time instant t = 0 h. Furthermore, the initial components of the tumor and healthy cells are distributed in space according to a smoothing function S:

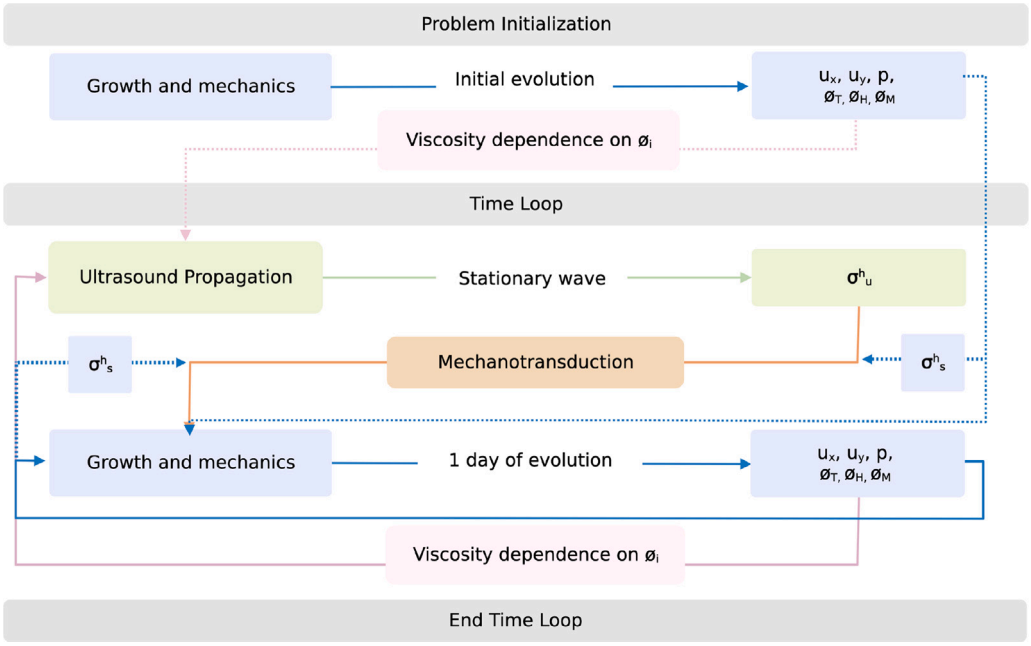

Fig. 2. Flowchart of the multiscale system. The system is initialized on a slow scale, where displacements, fluid pressure and solid phases are obtained. The solid phases are added to the fast-scale model of wave propagation to consider the viscosity of the tumor cell phase dependence, and it evolves until the stationary wave is achieved, where the ultrasonic hydrostatic stress is computed. Together with the slow hydrostatic stress, the ultrasonic stress is considered to compute the evolution of the system accounting for mechanotransduction. The results are again included at the slow and fast scale to complete the time loop until the final time of the simulations is achieved.

$$\begin{aligned} \phi_{T0} &= \overline{\phi}_{T0} S, \\ \phi_{H0} &= \overline{\phi}_{H0}\Big(1 - S\Big), \\ S &= \left[1 + e^{b_S \frac{(r - l_t)}{l}}\right]^{-1}, \end{aligned} \tag{21}$$

where the parameter $\overline{\phi}_{i0}$ is the initial concentration rate, l_t represents the tumor size, r the radial coordinate, and l the total length of the medium, while b_S is the smoothing coefficient, according to Ref. [26].

Regarding boundary conditions (BC), we adopt Winkler-inspired boundary conditions to consider tumor spheroid confinement at slow scales, $\boldsymbol{\sigma_n} = -k_w \mathbf{u}$, where $\mathbf{n}$ is the outer normal vector and k_w is a constant [30]. For fast-scale ultrasound propagation, we use the Lysmer–Kuhlemyer boundary condition to account for non-reflecting boundaries [45]. The normal stress reads $\boldsymbol{\sigma_n} = k_a \rho c_p \frac{\partial \mathbf{u}}{\partial t}$, where k_a is a constant in the range [0–100].

The numerical model is self-coded in FEAP 8.6 [46] considering two dimensions and plane strain. The problem is defined in Cartesian coordinates. The MATErial set command is used to specify the parameters for each material as well as to specify the element type associated with the material set parameters. First, we define an own-coded material, in which we defined the equations of the problem and set parameters. We then blend a square mesh with surface elements defined by quadrilateral (bilateral) shapes consisting of four nodes. The number of used elements depends on the dimensions and characteristics of the problem, ranging between 10^4 and $40 \cdot 10^4$. For the boundary conditions, line elements (2-node element) are defined using the standard FEAP element library. These are assigned with the FEAP materials: LABC for absorbing boundary conditions in wave propagation and WINKler for Winkler boundary conditions in the slow-scale model. The Newmark-β method with standard parameters is used as the numerical integration technique to solve the system of second-order differential equations while implicit Backward Euler integration is considered for first-order differential equations. The spatial discretization is performed with standard isoparametric shape functions of Lagrange type. We also employed Matlab (MathWorks Inc., Natick, MA, USA) to define the initial wave sent, and we visualized the results using Paraview [47]. The flowchart of the numerical simulations is reported in Fig. 2.

Furthermore, we propose modeling ultrasound propagation independently of its duty cycle, regardless of whether it is continuous or pulsed. By applying the mechanical wave throughout the cell growth process, we ensure a comprehensive analysis. This decision is motivated by the fact that the duty cycle operates on a millisecond timescale and is based on persistence. Consequently, once a mechanotransduction stimulus is applied, the corresponding cellular response persists for several seconds. Thus, even during the silent period of the duty cycle, signaling remains activated, enabling us to consider the stress field throughout the ultrasonic period. In addition, we compute the ultrasound wave until it reaches a stationary state, where stress levels remain constant regardless of

Table 1
Model parameters used in the simulations.

Description	Symbol	Data	Units	Reference
Young modulus	E	8	kPa	[26,40,48]
Undrained Poisson ratio	ν_u	0.49999	[–]	[40,48]
Drained Poisson ratio	ν	0.4	[–]	[30,40,48]
Mass density	ρ	1000	kg m^{-3}	Water
Hydraulic conductivity	k_h	$3.1 \cdot 10^{-14}$	m^2 Pa^{-1} s^{-1}	[33,40,48–50]
Biot coefficient	α	$9.91 \cdot 10^{-1}$	[–]	[26,51]
Biot modulus	M	1.79	MPa	[26,51]
Vessel conductivity	k_v	$2.70 \cdot 10^{-8}$	Pa^{-1} s^{-1}	[31,33,49]
Vessel pressure	p_v	$3.33 \cdot 10^{3}$	Pa	[33]
Reflection coefficient	ω	$9.00 \cdot 10^{-1}$	[–]	[31,49]
Interstitial osmotic pressure	$\pi_v - \pi_e$	$1.33 \cdot 10^{3}$	Pa	[31,49]
Lymphatic conductivity	k_{lo}	$9.98 \cdot 10^{-8}$	Pa^{-1} s^{-1}	[33]
Lymphatic vessel pressure	p_l	$1.33 \cdot 10^{2}$	Pa	[25]
Exchange coefficient	α_{TT}	1.30	[–]	[26]
Exchange coefficient	α_{TH}	1.00	[–]	[26]
Exchange coefficient	α_{TM}	1.00	[–]	[26]
Exchange coefficient	α_{HH}	3.00	[–]	[26]
Exchange coefficient	α_{HT}	2.00	[–]	[26]
Exchange coefficient	α_{HM}	1.00	[–]	[26]
ECM production from ϕ_T	β_T	$5.79 \cdot 10^{-7}$	s^{-1}	[26]
ECM production from ϕ_H	β_H	$1.16 \cdot 10^{-6}$	s^{-1}	[26]
ECM degradation from ϕ_T	$\delta_M \alpha_{MT}$	$2.89 \cdot 10^{-6}$	s^{-1}	[26]
ECM degradation from ϕ_H	$\delta_M \alpha_{MH}$	$2.89 \cdot 10^{-6}$	s^{-1}	[26]
Initial condition ϕ^T	ϕ^{T0}	$1.50 \cdot 10^{-1}$	[–]	[26]
Initial condition ϕ^H	ϕ^{H0}	$1.50 \cdot 10^{-1}$	[–]	[26]
Initial condition ϕ^M	ϕ^{M0}	$4 \cdot 10^{-1}$	[–]	[26]
Proliferation rate ϕ^T	T_T	$1.26 \cdot 10^{-5}$	s^{-1}	[26]
Proliferation rate ϕ^H	T_H	$1.26 \cdot 10^{-5}$	s^{-1}	[26]
Common lower rate	q	0.05	[–]	[26]
Mechanotransduction smoothness	χ_σ	−0.05	Pa^{-1}	[26]
Dynamic stress coefficient	β_u	0.2	[–]	Fitted
Tumoral threshold stress	σ_L	$1.2 \cdot 10^{3}$	Pa	[26,39–41]

the duration of the sonication. Through this methodology, we can effectively explore the implications of ultrasonic stress on the tumor microenvironment, unlocking its immense prospective as a promising avenue for cancer therapy.

The parameter values used in slow-scale simulations are summarized in Table 1 and the specific parameters for fast-scale ultrasound propagation include a range of frequencies between [1–20] MHz, acoustic pressures between [0.1–5] kPa, and viscosities between [0–10] Pa s. These frequencies and intensities ranges are well below those established by the FDA, which considerably minimizes the possibility of collateral damage (spatial-peak temporal-average intensity ISPTA < 100 mW cm^{-2}, and mechanical index MI < 1.9). In addition, we simplify the degrees of freedom of the system and adapt parameters in our experiment prediction.

We first reduce the degrees of freedom of the mathematical approach to fit the experimental data and reconstruct the mechanotransduction parameters. For simplicity, we have assumed the absence of the extracellular matrix and healthy phases, and we only consider the coexistence of proliferating tumor cells and fluid within the tumor spheroid, which means that $D_T = \alpha_{TH} = \alpha_{TM} = \Gamma_F = \Gamma_H = \Gamma_M = \beta_T = \beta_H = 0$. We have chosen specific mechanical parameters from the experiment, including a frequency of $f = 5$ MHz and an acoustic pressure of $A = 1.5$ kPa, while tumor and culture medium viscosity $\eta_T = 2$ Pa s, and $\eta_c = 0.05$ Pa s respectively, are assumed from the literature ranges [52].

To estimate the total number of cells, despite the lack of experimental cell count localization, we integrate the tumor phase over space at a given time, represented as $\int_A \phi_T(x, y, t) dA$. We calibrate the simulation parameters using data from the control experiment, which takes into account the observed deceleration of cell proliferation on the first day, attributed to the rearrangement and development of spheroid clusters. Therefore, the absence of significant differences between the control and sonication groups on the first day may be attributed to cellular reorganization. From the first day to the third day, a consistent and higher proliferation rate is maintained. Once the growth parameters are calibrated, we further adjust the mechanotransduction parameters to align with the experimental results.

In the numerical simulations detailed in Section 3.2, our methodology was grounded on established parameters, as listed in Table 1, to ensure the integrity and robustness of our findings. We specifically selected parameters related to mechanotransduction from experimental data, as these were not extensively covered in existing literature. To validate our model against a pre-existing system, we used previously established parameters as a starting point. This dual approach allowed us to incorporate novel experimental insights while ensuring our alignment of the model with validated scientific frameworks. While the cellular proliferation ratio was held constant, it is critical to acknowledge the inherently faster proliferation rate of tumor cells compared to healthy cells, which introduces complex dynamics regarding cellular competition. Modifications to the parameters T_T and T_H were systematically evaluated; however, these adjustments had negligible effects on the overall results. The proliferation rates remained within a narrowly defined range, indicating that the variations in these parameters did not significantly alter the qualitative or quantitative outcomes of the simulations.

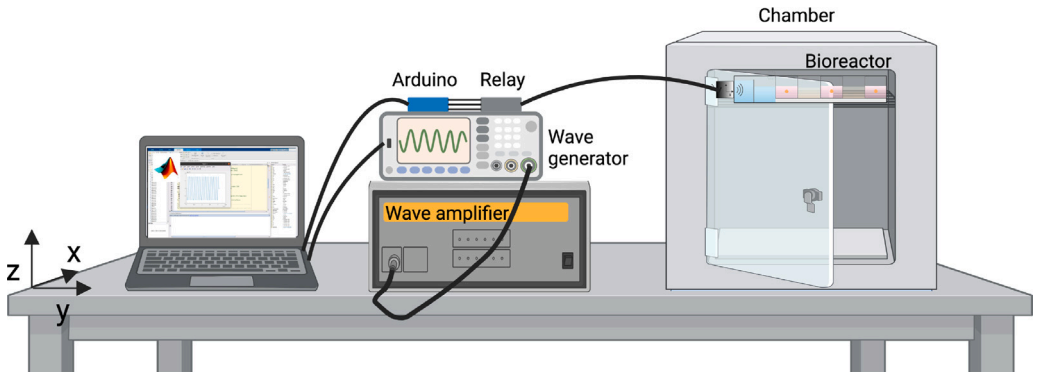

Fig. 3. Setup of the measurements. The Arduino is connected to the computer and the software is loaded, allowing the switch of mechanical signals. The Arduino also serves as a trigger to restart the signal and prevent any delay. The wave is generated using Matlab software and then loaded into the wave generator. Before connecting the wave generator to the amplifier, the signal is first verified using an oscilloscope to ensure that the frequencies and connections are correct. Once the signals have been tested, the transducer is connected and placed on the support, and the coupling gel is extended on the transducers and bioreactor faces as a coupling material to avoid air bubbles. The relays are then connected. As the final step, cells are transferred to their designated chambers in the bioreactor and placed in the incubator until subsequent analysis.

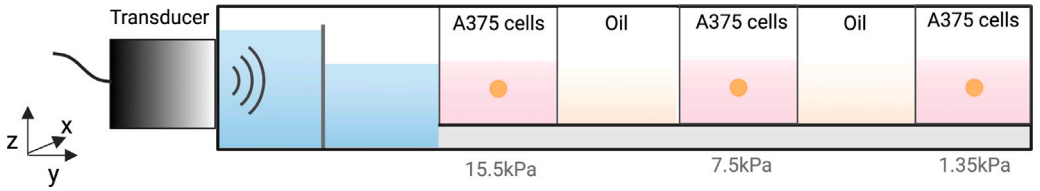

Fig. 4. Sonication scheme. The transducer emits an ultrasonic wave through the first medium of water, which prevents the temperature from increasing. The wave then travels through the culture containing cells and attenuating media, causing the acoustic pressure to decrease as it encounters different materials and viscosities. As a result, the same bioreactor can be used for a given frequency and various acoustic pressures.

2.3. Experimental setup

The experimental procedure involved a total of three replicates for each condition, namely the control group and the sonicated group. For each replication, three independent experiments are conducted.

The bioreactor in which the CSCs are located is subjected to a 70% alcohol spray and subsequently placed in a chamber designed for ultraviolet (UV) sterilization. This process lasts 30 min and ensures disinfection of the bioreactor by effectively eliminating possible contaminants with the use of UV light. The water and attenuating material chambers are filled with caution to prevent overflow and avoid any form of contamination or interference. In addition, the chambers are covered with insulating tape. The complete setup is shown in Fig. 3. To conduct the examination of cell proliferation, the bioreactor is removed from the incubator and moved to a UV sterilization chamber with laminar flow to avoid contamination.

The bioreactor used for cell culture consists of five sequentially arranged Petri dishes containing A-375 human melanoma cells embedded in a culture medium and an attenuating medium (oil), as depicted in Fig. 4. This experimental setup is designed to enable the generation of various wave amplitudes using a single transducer, as the emitted wave loses energy while propagating through different media. To prevent heating effects, a water-filled region is included at the beginning of the bioreactor. Acoustic pressure values are measured in each culture using a hydrophone probe, which is submerged in a replica of the bioreactor to capture acoustic pressure values without affecting tumor response. Through this method, we have determined that the first culture experiences 15.5 kPa, the second 7.5 kPa, and the third 1.35 kPa.

2.4. Cell culture

Melanoma cancer cell lines (A375) and fibroblasts were acquired from the American Type Culture Collection (ATCC) and were cultured according to the procedures recommended by the ATCC. Cell lines were passaged for a period of fewer than 6 months and were regularly tested for mycoplasma contamination. Cells were maintained in advanced DMEM (Sigma-Aldrich) supplemented with 10% FBS (Gibco) and 5% penicillin/streptomycin (Sigma-Aldrich).

To obtain tertiary spheres, cells were cultured in suspension using low-attachment plates containing DMEM-F12, 1% streptomycin-penicillin, 1 mg/mL hydrocortisone (Sigma-Aldrich), 4 ng/mL heparin (Sigma-Aldrich), 1X ITS (Gibco), 1X B27 (Gibco), 10 ng/mL EGF (Sigma-Aldrich), 10 ng/mL FGF (Sigma-Aldrich), 10 ng/mL HGF and 10 ng/mL IL6 (Miltenyi Biotec) as previously described [53]. Cells were cultured for 6 days and spheres are disaggregated every 72 h until tertiary spheres were

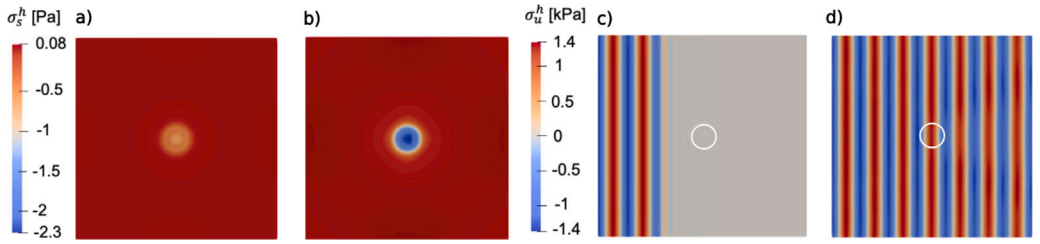

Fig. 5. Hydrostatic stresses during growth. (a) Slow hydrostatic stress of sonicated CSC at t = 1 day and (b) slow hydrostatic stress of sonicated CSC at t = 3 days. Slow hydrostatic compression increases at the center of the spheroid as it grows. (c) Fast ultrasound stress before reaching tumor spheroid and d) fast ultrasound stress when stationary state is achieved, where a slight decrease in stress is perceived after reaching the tumor spheroid. The main parameters for sonication are: frequency $f = 5$ MHz, $A = 1.5$ kPa, tumor viscosity $\eta_T = 2$ Pa s and culture medium viscosity $\eta_c = 0.05$ Pa s.

obtained. To achieve this, the spheres were collected by centrifugation at 1500 rpm for 5 min, incubated with trypsin-EDTA (Sigma-Aldrich) at 37 °C for 5 min, and then inactivated with FBS. The cells were then washed with PBS and reseeded under the same culture conditions. After that, melanospheres CSC and fibroblasts phenotype was confirmed as previously described [53].

2.5. Cell proliferation assay

Alamar Blue Assay (Biorad) was the measurement method. Cell growth was monitored on days 0, 1, and 3. To ensure reliable results, two parallel experiments were conducted. In the first experiment, a bioreactor loaded with melanoma CSCs was exposed to 24 h of ultrasound and measurements were taken. In the second experiment, a bioreactor was used in which cells were treated for 72 h without interruption. This approach was implemented to avoid any possible interference or damage during the manipulation of the spheroids.

The experimental protocol consisted of adding 10 µl of Alamar Blue solution per 100 µl of media to the cells and incubating them for 2 h. Following the incubation period, the fluorescence intensity was measured using the Synergy HT instrument (BIO-TEK) at an excitation wavelength of 530 nm and emissions of 590 nm. For the data analysis, a non-parametric methodology was developed under the assumption of non-normality in the growth rate variables and the small size of the samples. The Kruskal–Wallis with Wilcox proves were performed for pairwise comparisons between group levels with corrections for multiple testing. RStudio software Version 1.4.1717 has been used to analyze the statistical differences. Although no apoptosis assays were performed in this study, we strongly encourage future research to include them to gain a more complete understanding of the underlying cellular processes.

3. Results

3.1. LIUS hinders CSC growth in-vitro

Melanoma CSCs are insonified at a frequency of 5 MHz, enabling partial tumor penetration and enhanced mechanotransduction without cytoskeleton damage. Our experimental results yielded safe acoustic pressure values of 1.35 kPa, 7.5 kPa, and 15.5 kPa, inducing mechanotransduction effectively without the tissue disruption associated with higher pressures.

In our experiments, we observed a significant decrease in the net proliferation of CSCs when subjected to 5 MHz sonication, as compared to the control spheroids, over a three-day period ($p = 0.018$, Wilcoxon-Mann–Whitney test). However, no significant differences were found among the different acoustic pressures. These results suggest that the sensitivity limit of cells may have been reached before reaching 1.5 kPa, supporting the hypothesis that cells have a lower sensitivity limit for dynamic stress compared to static stress [25,26,32,39].

The mathematical model used to explain experiments is described in Methods in the framework of the infinitesimal growth, poroelasticity theory [25,26,28,40] and a multiscale approach [27,29].

From a computational standpoint, the hydrostatic stresses characterizing the stress state of the tumor manifest themselves at two distinct scales: the slow and ultrasonic stress, as depicted in Fig. 5. With regard to slow-scale stress, compression is predominantly concentrated in the core of the tumor and consistent with previous research [54–56]. Additionally, this study also points out that the compression state increases over time and growth and operates at the order of Pascals, whereas ultrasound stress, which is defined by rarefaction and compression, is three orders of magnitude bigger. Such a substantial difference in stress scales implies that ultrasound stress is expected to exert a more prominent impact on mechanotransduction than the slow-scale stress.

Furthermore, numerical simulations suggest that ultrasound diffraction through the tumor can result in slight shadow areas with lower displacements and stresses. For this particular case study, the slight diffraction presented is attributed to the difference in viscosity between the culture medium and the tumor spheroid at the applied frequency, resulting in a heterogeneous stress distribution within the bioreactor.

The propagation patterns of mechanical waves impact mechanotransduction processes. Computational analysis (Fig. 6) reveals that the mechanotransduction function $\mathcal{M}_T$ – a mathematical relationship that describes how stress affects tumor growth – remains

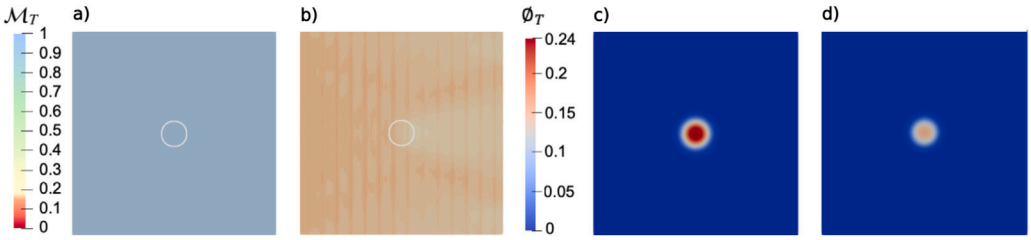

Fig. 6. Mechanotransduction and growth. (a) Control culture exhibits constant mechanotransduction values in space. (b) Dynamic LIUS hydrostatic stress causes shadow areas that are translated into patterns in the mechanotransduction function. (c) The control culture demonstrates a pronounced tumoral phase (ϕ_T), representing a substantial fraction of tumor cells within the media composition. d) In comparison to the control cells, the sonicated cells exhibit attenuated proliferation, indicating a decrease in their growth rate. The main parameters used for these simulations are $\alpha_{TT} = 2.9$, $\beta = 0.2$, $t = 3$ days. The US parameters are $A = 1.5$ kPa, $f = 5$ MHz, $\eta_T = 2$ Pa s and $\eta_c = 0.05$ Pa s.

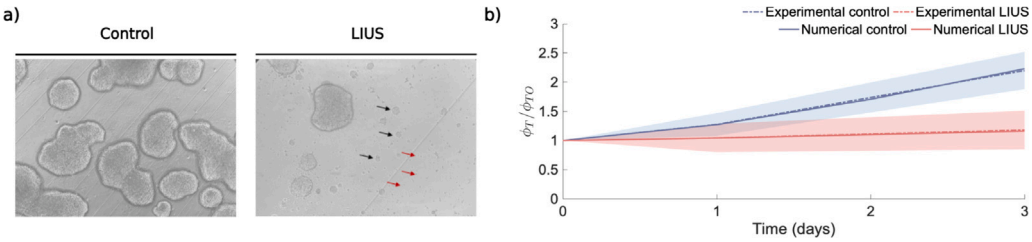

Fig. 7. Reduction in cell viability for sonicated tumor spheroids at frequency $f = 5$ MHz, $A = 1.5$ kPa, tumor viscosity $\eta_T = 2$ Pa s and culture medium viscosity $\eta_c = 0.05$ Pa s (a) Visualization of melanospheres with optical microscopy, where comparative analysis of untreated control and 5 MHz treated melanospheres after 72 h is shown. Reduced-sized melanospheres are indicated by black arrows, while red arrows highlight individual cells. Images captured at 10x magnification. (b) Computational model of LIUS mechanotherapy reproduces in vitro experiments. The dashed lines represent experiments, and the shaded bands their interval of confidence, while the solid lines denote numerical simulations. A trend change is observed between the control and sonicated cells, where cell proliferation decreases 48% on the third day after the application of LIUS. The proliferation parameters used are $T_T = 0.58 \cdot 10^{-5}$ s^{-1} on the first day and $T_T = 0.77 \cdot 10^{-5}$ s^{-1} from day one, while $\alpha_{TT} = 2.9$. The mechanotransduction parameters are $q_T = 0.05$, $b_T = 0.05$, $\beta_u = 0.2$, and $\sigma_{L_T} = 1.2$ kPa.

spatially constant in the control culture. This is attributed to the total stress generated during the 3-day growth period remaining below the threshold stress of tumor cells for the duration of ultrasonic exposure, resulting in unaffected growth. On the other hand, ultrasound diffraction introduces spatial heterogeneity in mechanotransduction. Our numerical observations suggest that the resulting stress shadow is inadequate to elicit discernible growth or migration patterns in cells via pressure gradients towards regions of lower stress.

Therefore, the numerical results support a homogeneous decrease in tumor cell proliferation following sonication at a frequency of $f = 5$ MHz relative to the control experiments, aligning with the proposed mechanotransduction mechanism.

Fig. 7a clearly demonstrates that subjecting melanospheres to a 5 MHz frequency for 72 h led to a significant decrease in both the number and size of the spheroids. Additionally, ultrasound had an adverse impact on cell viability, resulting in the identification of non-viable individual cells due to the induced disaggregation and toxic effects of LIUS.

The numerical simulations presented in this study closely replicate the initial experimental observations, as illustrated in Fig. 7b. Despite the challenges of experimental cell count localization, our estimation method, based on integrating the tumor phase over space, provides insights into the overall cell population. By comparing the estimated cell count with experimental findings, we validate the accuracy of our simulation. Additionally, the calibration of simulation parameters using the control experiment data ensures the reliability of our results. The adjusted mechanotransduction parameters further enhance the agreement between our simulations and experimental outcomes.

In addition, we present a sensitivity analysis investigating the influence of frequencies, acoustic pressures, and viscosities on the behavior of tumor dynamics under various mechanical wave conditions. The key findings of the sensitivity analysis, summarized concisely in Table 2, provide valuable insights into the impact of different mechanical wave parameters on tumor proliferation rates. Our numerical simulations demonstrate that acoustic pressures greater than 1.5 kPa can produce substantial reductions in proliferation rates ranging from 46.6% to 48% for frequency values within the range of 1–5 MHz. Interestingly, these reductions occur when the viscosity of the medium is $\eta_c = 0.05$ Pa s, indicating that the perceived limitations of CSCs can be reached before surpassing this acoustic pressure threshold. For higher frequency values, such as 20 MHz, an increase in acoustic pressure of 5 kPa is required to achieve a 52.5% decrease in proliferation rates. Furthermore, the influence of medium viscosity is observed, as higher viscosities result in increased wave attenuation, potentially limiting the reduction in proliferation rates and leading to values comparable to those of the control group (0–39.6% reduction compared to non-sonicated cells).

These findings and bioeffects align with previous research, as succinctly summarized in Table 3, where mechanotransduction studies typically involve frequencies ranging from 0.3 to 1.5 MHz. Notably, our study deviates with a higher frequency of 5

Table 2
Numerical results of LIUS therapy and proliferation reduction of CSCs in comparison to the control group on the third day.

f [MHz]	A [kPa]	η_c [Pa s]	η_T [Pa s]	Proliferation decrease [%]
1	1.5	0.05	2	48.4
5	1.5	0.05	2	48
20	1.5	0.05	2	27.3
20	5	0.05	2	52.5
5	0.1	0.05	2	0.0
5	0.5	0.05	2	38.1
5	3	0.05	2	50.7
5	1.5	0.05	5	47.5
5	1.5	0.05	10	46.6
5	1.5	2	0.05	39.6
5	1.5	5	0.05	14.8
5	1.5	10	0.05	0.21

Table 3
Main setups in LIUS cancer therapy in vitro. The relation between intensity and acoustic pressure has been established.

Cell line	Frequency [MHz]	Intensity [m W/cm^2]	Acoustic pressure [MPa]	Setup and Comments	Bioeffects	N	Source
CT-26, K562, U937, T cell (in suspension)	0.3–0.67	$<9.7 \cdot 10^4$	<1.2	TUS = 2 min/day for 2 days. PD = 2–40 ms. DC = 10%. Requires standing waves and reflection	Cytodisruption. Selective growth inhibition	3–9	[6]
T47D, MCF-12A (monolayers)	1.5	10,30, 50,100	0.012, 0.021, 0.027, 0.039	TUS = 10 min/day for 3 days. PD = 200 μs. DC = 20%. Decreasing proliferation with increasing intensity, PD, and DC.	Mechanotransduction. Selective growth inhibition	1	[12]
HT29, Caco2	0.65–4.5	$87.4–6.7 \cdot 10^4$	0.036–1	TUS = 10 min/day for 1 day. PD = 30 s. DC = 25%	Mechanotransduction - Cytodisruption. Growth inhibition	2	[10]
MDA-MB-231, Raw-264.7	1.5	30	0.021	TUS = 20 min/day for 10 days. PD = 200 μ. DC = 20%	Mechanotransduction. Reduction of osteoclastic differentiation	3	[13]
A375, A549, Hela, Hacat	0.67	254	0.061	TUS = 2 min for 2 days, PD = 30 ms, DC = 10%. Importance of stress field distribution.	Mechanotransduction - Cytodisruption. Selective growth inhibition	[–]	[9]
MDA-MB-231, A375P, HT180	0.33	7.7	0.011	TUS = 2 h/day for 3 days. PD = [–]. DC = 50%	Mechanotransduction: Piezo1 channel. Growth inhibition	2–3	[16]
MDA-MB-231, MCF10A (monolayers in matrigel)	0.33	7.7	0.011	TUS = 2 h/day for 3 days. PD = [–]. DC = 50%. Growth inhibition	Mechanotransduction: Piezo1 channel. Growth inhibition	4	[15]
PANC-1 (monolayers)	1	<100	0.038	TUS = 10-20-30 min. DC = 100%	Mechanotransduction. Migration inhibition	4	[14]

MHz, accompanied by substantially lower intensities around 5 kPa while achieving similar bioeffects. Furthermore, our parameters suggest that we are operating beyond the threshold of cytodisruption. Consequently, our results substantiate the hypothesis that comparable reductions in proliferation rates can be attained by applying lower levels of dynamic stress and higher frequencies, thereby reinforcing the effectiveness of these strategies for treating cancer stem cells. Additionally, we have reported a 50% reduction in proliferation rates compared to stress-free growth under static stress conditions, corroborating findings from prior studies [25,26,39–41,57].

Although not the primary focus, we also tested healthy primary dermal fibroblasts to evaluate their response to the insonification parameters used in our main experiments. As reported in the literature [6,9,12], these supplementary tests confirmed that fibroblasts

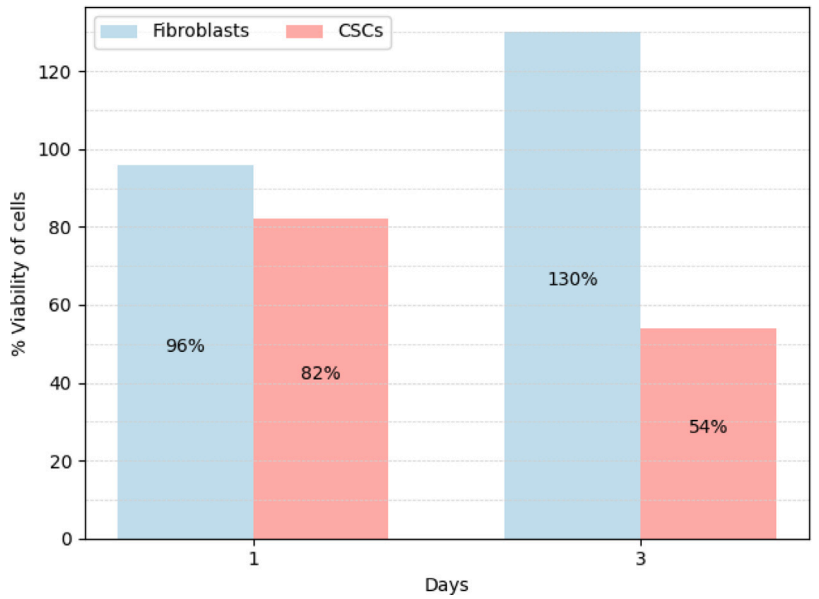

Fig. 8. Viability of cells after sonication. Viability of cells expressed as a ratio between the control cells and the sonicated cells. The blue bars indicate the viability of fibroblasts insonified at 5 MHz, while the red data show the survival ratio of CSCs. The results are shown for the first and third day of experiments. (For interpretation of the references to color in this figure legend, the reader is referred to the web version of this article.)

did not exhibit significant inhibition when exposed to 5 MHz at any amplitude. Fig. 8 compares the effects of 5 MHz ultrasound on fibroblasts and CSCs, showing significant differences in their dynamic behavior. Indeed, fibroblast activity increased by 32% compared to the control on the third day, contrasting with a 54% reduction in CSCs, supporting our analysis and aligning with previous findings on ultrasound for wound healing [58–61]

3.2. LIUS causes selective patterns

To broaden the scope of our study, explore a wider range of phenomena, and gain a deeper understanding of the underlying mechanisms at play, we extend our research from the micro-scale to the macro-scale. Thus we propose to apply LIUS to a previously validated mathematical model, see [26]. For these simulations, we use all the equations described in Methods and the mechanotransduction parameters fitted to our experimental data. We investigate the potential of 1 MHz ultrasound as a selective modification tool for cancer cells with viscosities of 5 Pa s.

Our simulations (Fig. 9) reveal that ultrasound does not directly affect the proliferation and production of healthy cells. Stress experienced by healthy cells is considerably lower than that experienced by tumor cells, suggesting that ultrasound selectively attacks cancer cells, as reported in [6,9,12]. We analyze the interplay of tumor and healthy cell growth, influenced by predator–prey dynamics. Our results confirm a decrease in tumor cell growth that affects healthy cells without impacting their overall proliferation due to a higher proliferation threshold ($\sigma_L \geq 10$ kPa and $\beta_u = 0.2$).

Furthermore, the existence of areas characterized by varying stress levels can trigger instabilities within tumors. This process disrupts their initial symmetry resulting in the concentration of cells in regions with low levels of stress and generating patterns as experimentally studied in [9]. The patterns are transmitted to the ECM phase, breaking into its homogeneous growth and possibly inducing its remodeling.

The computational results also suggest that LIUS decreases tumor migration compared to nonsonicated cells, which is in agreement with the experimental results obtained in [14]. Additionally, the results indicate that healthy cells and the extracellular matrix exhibit an adaptive growth response to cancer phase motility through predator–prey dynamics. Thus, the movement of tumor cells induces or influences the movement of healthy cells and ECM [62–64], as it is shown in *Supplementary Material Video S1*. Furthermore, migration dissipates and homogenizes differences in growth patterns while keeping a predetermined direction of tumor cell concentration.

These observations provide a suitable explanation for the persistent proliferation of cells observed in certain experimental studies. Tumor cells may have the ability to proliferate in areas known as shadow zones, where the stress threshold is reached heterogeneously, resulting in a total cell count comparable to that of the control group. Considering motility, leader cancer cells located in low stress areas have the capacity to enhance migration, probably through the use of their cytonemes that sense and respond to the stress state of the surrounding environment [35,65], allowing them to retract from high stress areas.

In fact, if tumor viscosity increases (see Fig. 10), cells tend to concentrate in areas of lower stress, displacing the center of the tumor phase in the direction of wave propagation. Furthermore, the presence of cell mobility leads to a decrease in overall cell concentration but an increase in dispersion.

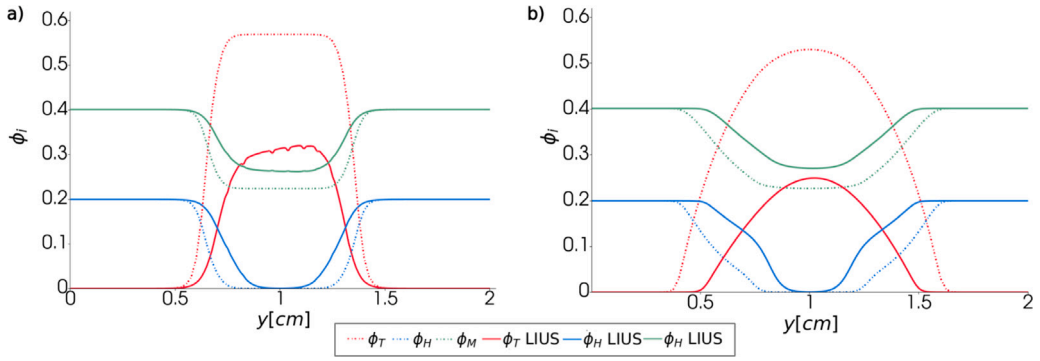

Fig. 9. Patterns in growth and migration. Dashed lines refer to tumor dynamics without sonication while solid lines refer to a sonicated tumor phase. (a) When migration is not allowed, LIUS selectively reduces tumor cell phase proliferation, causing patterns in low-stress areas that translate to ECM phase while healthy phase remains unaltered. (b) Tumor phase migration is reduced by LIUS sonication while it dampens patterns of low-stress areas, keeping the direction of tumor cell phase concentration. The used parameters are $f = 1$ MHz, $A = 1.5$ kPa, and $\eta_T = 5$ Pa s. Results at time $t = 21$ days. We refer to *Supplementary Material Video S2* for the animation.

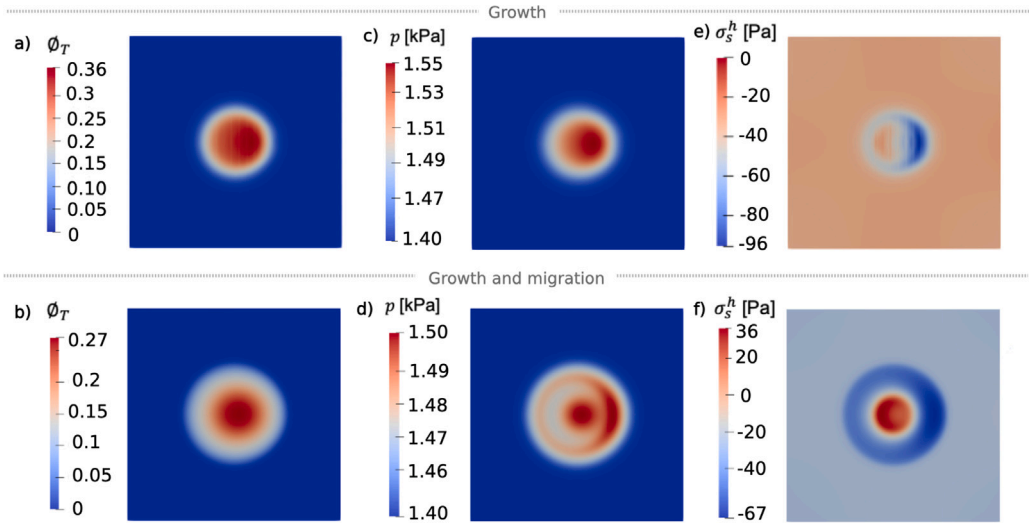

Fig. 10. Tumor phase, interstial fluid pressure, and slow stress after LIUS sonication. Tumor phase, IFP and slow stress increase in the direction of wave propagation, while migration homogenizes the response of the tumor dynamics. The main parameters used for these simulations are $\eta_T = 10$ Pa s, $f = 1$ MHz, $A = 1.5$ kPa. Results are shown for $t = 21$ days. We refer to *Supplementary Material Video S3* for the animation.

Interstitial fluid pressure increases during tumor growth, resulting in an uneven distribution of pressure. This pressure gradient could compress blood vessels, hindering the delivery of nutrients and drugs to tumor cells [20,33,66], while migration aids in stress dissipation and mitigates the substantial elevation of interstitial pressure observed when migration is disregarded [35]. Likewise, the growth of a sonicated tumor generates a slow and gradual increase in stress, although it is relatively minor compared to controlled growth conditions, while compression occurs predominantly in the direction of tumor expansion, aligning with the preferred migration pathway.

4. Discussion

In this investigation, we unveil a theoretical framework to elucidate the potential mechanism through which LIUS selectively targets cancer stem cells. Merging computer simulations rooted in a mechanically coupled mathematical model of tumor spheroids with experimental validation, our results showcase that LIUS initiates a stress condition, strategically impeding and partially inhibiting tumor growth.

Our numerical findings also demonstrate that ultrasound induces a significantly compressive hydrostatic stress state within the spheroid, creating shadow areas due to viscosity differences between the medium and the tumor spheroid.

The proposed model considers the growth and migration of a poroelastic tumor, and the selection of strategic parameters based on the feedback with our experimental results. This allows us to address the possible challenges related to the prediction,

controllability, and guidance of new experiments, while effectively avoiding effects associated with cavitation, cytodisruption and standing waves [6–11]. Regarding the complex interplay between LIUS and cancer dynamics, our study confirm that ultrasound does not directly affect healthy cell proliferation and production. Instead, ultrasound selectively targets cancer cells, minimizing adverse effects on surrounding healthy tissue. We show that reductions in proliferation rates can be achieved by applying lower levels of dynamic stress, reinforcing the potential of these strategies for cancer stem cell treatment. Likewise, our data allow us to conclude that LIUS decreases tumor migration, generating specific growth patterns. An increase in tumor viscosity or frequency leads to greater wave attenuation, resulting in wave diffraction that creates shadow areas with minor displacements and stresses, where the tumor cells are more prone to concentrating, growing, and migrating. These differences may help explain why, at times, the total cell count does not decrease compared to non-sonicated cells.

Then, our interdisciplinary study provides a promising approach to exploring the effects of LIUS mechanotherapy on cancer stem cells, showing agreement with the previously known experimental results, and with the experiments developed for this paper. Future studies could explore creating spheroids comprising both tumor and healthy cells to investigate combined selectivity. Finally, additional validation using both longitudinal and shear waves [20,67,68] is necessary to confirm the selectivity of the attack. Once validated and refined, the model has the potential to bring about a significant transformation in the clinical approach to cancer treatment. Then, our results open up new prospects for further development and experimentation, and this LIUS strategy could offer a less aggressive effects on surrounding healthy tissue, more effective, and cost-effective treatment option for cancer stem cells. In the long run, integrating patient information, big data and artificial intelligence [69] holds the promise of tailoring LIUS-based treatments to individual patients, thus optimizing their effectiveness.

CRediT authorship contribution statement

Beatriz Blanco: Conceptualization, Formal analysis, Methodology, Software, Validation, Writing – original draft, Writing – review & editing. **Roberto Palma:** Conceptualization, Formal analysis, Investigation, Software. **Manuel Hurtado:** Data curation, Investigation, Visualization. **Gema Jiménez:** Data curation, Investigation, Visualization. **Carmen Griñán-Lisón:** Data curation, Investigation, Visualization. **Juan Melchor:** Conceptualization, Data curation, Methodology, Validation. **Juan Antonio Marchal:** Conceptualization, Data curation, Methodology, Supervision. **Hector Gomez:** Conceptualization, Formal analysis, Investigation, Software, Methodology, Supervision . **Guillermo Rus:** Conceptualization, Formal analysis, Investigation, Methodology, Resources, Software, Validation, Project administration, Supervision . **Juan Soler:** Conceptualization, Formal analysis, Funding acquisition, Investigation, Methodology, Project administration, Supervision, Writing – review & editing.

Acknowledgments

This study was funded by Ministry of Science, Innovation and Universities of Spain, project numbers PID2020-115372RB-I00 (B.B., M.H. and G.R.), PID2022-137228OB-I00 (MICIU/AEI /10.13039/501100011033) (J.S.), by Modeling Nature Research Unit, Grant QUAL21-011 funded by Consejería de Universidad, Investigación e Innovación (Junta de Andalucía) (J.S.,B.B., M.H., G.R., G.J, C.G and J.A.M), Consejería de Innovación, Ciencia *y* Empresa, Junta de Andalucía A-CTS-180-UGR20 (G.J, C.G and J.A.M.), B-FQM-580-UGR20 (B.B., J.S.), and by Consejería de Universidad, Investigación e Innovación from Junta de Andalucía, P21.00182 (B.B., M.H. and G.R.). This paper has been partially supported by the MINECO-FEDER (Spain) research grant number EQC2021-006920-P (J.A.M.) and PID2019-106947RA-C22 (B.B., J.M. and G.R.) and from the Chair 'Doctors Galera-Requena in cancer stem cell research' (CMC-CTS963). G.J. and C.G. acknowledge the posdoctoral fellowship from Plan Andaluz de Investigación, Desarrollo e Innovación (PAIDI 2020—FEDER funds—). Lastly, B.B. research was supported by the Ministry of Science, Innovation and Universities of Spain, FPU17/01415. Under grant 101096884, Listen2Future is co-funded by the European Union. Views and opinions expressed are however those of the author(s) only and do not necessarily reflect those of the European Union or Key Digital Technologies Joint Undertaking. Neither the European Union nor the granting authority can be held responsible for them. The project is supported by the Key Digital Technologies Joint Undertaking and its members including top-up funding by Austria, Belgium, Czech Republic, Germany, Netherlands, Norway, and Spain. Figures of SI were created with Biorender.com.

Code availability

The codes that support the plots within this paper are described in the Methods, and they are available from the corresponding authors upon request.

Appendix A. Supplementary data

Supplementary material related to this article can be found online at https://doi.org/10.1016/j.matcom.2024.08.030.

References

[1] D. Huang, S. Kidoaki, Stiffness-optimized drug-loaded matrix for selective capture and elimination of cancer cells, J. Drug Deliv. Sci. Technol. 55 (2020) 101414.
[2] R.K. Jain, T. Stylianopoulos, Delivering nanomedicine to solid tumors, Nat. Rev. Clin. Oncol. 7 (11) (2010) 653.
[3] C. Polydorou, F. Mpekris, P. Papageorgis, C. Voutouri, T. Stylianopoulos, Pirfenidone normalizes the tumor microenvironment to improve chemotherapy, Oncotarget 8 (15) (2017) 24506.
[4] M. Panagi, F. Mpekris, P. Chen, C. Voutouri, Y. Nakagawa, J.D. Martin, T. Hiroi, H. Hashimoto, P. Demetriou, C. Pierides, et al., Polymeric micelles effectively reprogram the tumor microenvironment to potentiate nano-immunotherapy in mouse breast cancer models, Nature Commun. 13 (1) (2022) 7165.
[5] M.H. Abedi, M.S. Yao, D.R. Mittelstein, A. Bar-Zion, M.B. Swift, A. Lee-Gosselin, P. Barturen-Larrea, M.T. Buss, M.G. Shapiro, Ultrasound-controllable engineered bacteria for cancer immunotherapy, Nature Commun. 13 (1) (2022) 1585.
[6] D.R. Mittelstein, J. Ye, E.F. Schibber, A. Roychoudhury, L.T. Martinez, M.H. Fekrazad, M. Ortiz, P.P. Lee, M.G. Shapiro, M. Gharib, Selective ablation of cancer cells with low intensity pulsed ultrasound, Appl. Phys. Lett. 116 (1) (2020) 013701.
[7] S. Heyden, M. Ortiz, Oncotripsy: Targeting cancer cells selectively via resonant harmonic excitation, J. Mech. Phys. Solids 92 (2016) 164–175.
[8] S. Heyden, M. Ortiz, Investigation of the influence of viscoelasticity on oncotripsy, Comput. Methods Appl. Mech. Engrg. 314 (2017) 314–322.
[9] J. Lin, S. Dong, W. Peng, H. Liu, P. Zhang, H. Lv, L. Yu, C. Yao, Low-intensity pulsed ultrasound for killing tumor cells: The physical and biological mechanism, 2022, pp. 812–820.
[10] D. Lucchetti, L. Perelli, F. Colella, C. Ricciardi-Tenore, G.L. Scoarughi, G. Barbato, A. Boninsegna, R. De Maria, A. Sgambato, Low-intensity pulsed ultrasound affects growth, differentiation, migration, and epithelial-to-mesenchymal transition of colorectal cancer cells, J. Cell. Physiol. 235 (6) (2020) 5363–5377.
[11] P. Prentice, A. Cuschieri, K. Dholakia, M. Prausnitz, P. Campbell, Membrane disruption by optically controlled microbubble cavitation, Nat. Phys. 1 (2) (2005) 107–110.
[12] A. Katiyar, J. Osborn, M. DasBanerjee, L.G. Zhang, K. Sarkar, K.P. Sarker, Inhibition of human breast cancer cell proliferation by low-intensity ultrasound stimulation, J. Ultrasound Med. 39 (10) (2020) 2043–2052.
[13] V. Carina, V. Costa, S. Pagani, A. De Luca, L. Raimondi, D. Bellavia, S. Setti, M. Fini, G. Giavaresi, Inhibitory effects of low intensity pulsed ultrasound on osteoclastogenesis induced in vitro by breast cancer cells, J. Exp. Clin. Cancer Res. 37 (1) (2018) 1–11.
[14] I. González, J. Luzuriaga, A. Valdivieso, J. Frutos, J. López, L. Hernández, L.M. Rodríguez-Lorenzo, V. Yagüe, J.L. Santiago Blanco, A. Pinto, et al., Low-intensity continuous ultrasound to inhibit cancer cell migration, Front. Cell Dev. Biol. (2023).
[15] A. Singh, A. Tijore, F. Margadant, C. Simpson, D. Chitkara, B.C. Low, M. Sheetz, Enhanced tumor cell killing by ultrasound after microtubule depolymerization, BioEng. Transl. Med. 6 (3) (2021) e10233.
[16] A. Tijore, F. Margadant, M. Yao, A. Hariharan, C.A.Z. Chew, S. Powell, G.K. Bonney, M. Sheetz, Ultrasound-mediated mechanical forces selectively kill tumor cells, 2020, BioRxiv.
[17] S. Na, O. Collin, F. Chowdhury, B. Tay, M. Ouyang, Y. Wang, N. Wang, Rapid signal transduction in living cells is a unique feature of mechanotransduction, Proc. Natl. Acad. Sci. 105 (18) (2008) 6626–6631.
[18] B. Geiger, J.P. Spatz, A.D. Bershadsky, Environmental sensing through focal adhesions, Nature Rev. Mol. Cell Biol. 10 (1) (2009) 21–33.
[19] V. Vogel, Mechanotransduction involving multimodular proteins: converting force into biochemical signals, Annu. Rev. Biophys. Biomol. Struct. 35 (2006) 459–488.
[20] B. Blanco, H. Gomez, J. Melchor, R. Palma, J. Soler, G. Rus, Mechanotransduction in tumor dynamics modeling, Phys. Life Rev. 44 (2023) 279–301.
[21] F. Broders-Bondon, T.H.N. Ho-Bouldoires, M.-E. Fernandez-Sanchez, E. Farge, Mechanotransduction in tumor progression: the dark side of the force, J. Cell Biol. 217 (5) (2018) 1571–1587.
[22] D.B. Agus, F. Michor, The sciences converge to fight cancer, Nat. Phys. 8 (11) (2012) 773–774.
[23] S. Colak, J.P. Medema, Cancer stem cells–important players in tumor therapy resistance, FEBS J. 281 (21) (2014) 4779–4791.
[24] M.A. Olivares-Urbano, C. Griñán-Lisón, J.A. Marchal, M.I. Núñez, CSC radioresistance: A therapeutic challenge to improve radiotherapy effectiveness in cancer, Cells 9 (7) (2020) 1651.
[25] A. Carotenuto, A. Cutolo, A. Petrillo, R. Fusco, C. Arra, M. Sansone, D. Larobina, L. Cardoso, M. Fraldi, Growth and in vivo stresses traced through tumor mechanics enriched with predator-prey cells dynamics, J. Mech. Behav. Biomed. Mater. 86 (2018) 55–70.
[26] A.R. Carotenuto, A. Cutolo, S. Palumbo, M. Fraldi, Lyapunov stability of competitive cells dynamics in tumor mechanoBiol, Acta Mech. Sin. 37 (2) (2021) 244–263.
[27] G. Rus, Nature of acoustic nonlinear radiation stress, Appl. Phys. Lett. 105 (12) (2014) 121904.
[28] M.A. Biot, General theory of three-dimensional consolidation, J. Appl. Phys. 12 (2) (1941) 155–164.
[29] J.K. Kevorkian, J.D. Cole, Multiple Scale and Singular Perturbation Methods, vol. 114, Springer Science & Business Media, 2012.
[30] G. Lorenzo, T.J. Hughes, P. Dominguez-Frojan, A. Reali, H. Gomez, Computer simulations suggest that prostate enlargement due to benign prostatic hyperplasia mechanically impedes prostate cancer growth, Proc. Natl. Acad. Sci. 116 (4) (2019) 1152–1161.
[31] M. Wu, H.B. Frieboes, S.R. McDougall, M.A. Chaplain, V. Cristini, J. Lowengrub, The effect of interstitial pressure on tumor growth: coupling with the blood and lymphatic vascular systems, J. Theoret. Biol. 320 (2013) 131–151.
[32] M. Fraldi, A.R. Carotenuto, Cells competition in tumor growth poroelasticity, J. Mech. Phys. Solids 112 (2018) 345–367.
[33] T. Stylianopoulos, J.D. Martin, M. Snuderl, F. Mpekris, S.R. Jain, R.K. Jain, Coevolution of solid stress and interstitial fluid pressure in tumors during progression: implications for vascular collapse, Cancer Res. 73 (13) (2013) 3833–3841.
[34] M. Conte, S. Casas-Tintò, J. Soler, Modeling invasion patterns in the glioblastoma battlefield, PLoS Comput. Biol. 17 (1) (2021) e1008632.
[35] B. Blanco, J. Campos, J. Melchor, J. Soler, Modeling interactions among migration, growth and pressure in tumor dynamics, Mathematics 9 (12) (2021) 1376.
[36] J. Calvo, J. Campos, V. Caselles, Ó. Sánchez, J. Soler, Qualitative behaviour for flux-saturated mechanisms: travelling waves, waiting time and smoothing effects, J. Eur. Math. Soc. 19 (2) (2017) 441–472.
[37] J. Calvo, J. Campos, V. Caselles, O. Sánchez, J. Soler, Pattern formation in a flux limited reaction–diffusion equation of porous media type, Invent. Math. 206 (1) (2016) 57–108.
[38] B.D. Hoffman, C. Grashoff, M.A. Schwartz, Dynamic molecular processes mediate cellular mechanotransduction, Nature 475 (7356) (2011) 316–323.
[39] G. Helmlinger, P.A. Netti, H.C. Lichtenbeld, R.J. Melder, R.K. Jain, Solid stress inhibits the growth of multicellular tumor spheroids, Nature Biotechnol. 15 (8) (1997) 778.
[40] T. Roose, P.A. Netti, L.L. Munn, Y. Boucher, R.K. Jain, Solid stress generated by spheroid growth estimated using a linear poroelasticity model, Microvasc. Res. 66 (3) (2003) 204–212.
[41] G. Cheng, J. Tse, R.K. Jain, L.L. Munn, Micro-environmental mechanical stress controls tumor spheroid size and morphology by suppressing proliferation and inducing apoptosis in cancer cells, PloS ONE 4 (2) (2009) e4632.
[42] A.S. Dukhin, P.J. Goetz, Bulk viscosity and compressibility measurement using acoustic spectroscopy, J. Chem. Phys. 130 (12) (2009) 124519.

[43] L. Claes, R.S. Chatwell, E. Baumhögger, T. Hetkämper, H. Zeipert, J. Vrabec, B. Henning, Measurement procedure for acoustic absorption and bulk viscosity of liquids, Measurement 184 (2021) 109919.
[44] F.T. d'Astous, F.S. Foster, Frequency dependence of ultrasound attenuation and backscatter in breast tissue, Ultrasound Med. Biol. 12 (10) (1986) 795–808.
[45] J. Lysmer, R.L. Kuhlemeyer, Finite dynamic model for infinite media, J. Eng. Mech. 95 (4) (1969) 859–877.
[46] R.L. Taylor, FEAP - Finite element analysis program, 2014, URL http://www.ce.berkeley/feap.
[47] J. Ahrens, B. Geveci, C. Law, ParaView: An end-user tool for large data visualization, in: Visualization Handbook, Elesvier, ISBN: 978-0123875822, 2005.
[48] P.A. Netti, D.A. Berk, M.A. Swartz, A.J. Grodzinsky, R.K. Jain, Role of extracellular matrix assembly in interstitial transport in solid tumors, Cancer Res. 60 (9) (2000) 2497–2503.
[49] R.K. Jain, R.T. Tong, L.L. Munn, Effect of vascular normalization by antiangiogenic therapy on interstitial hypertension, peritumor edema, and lymphatic metastasis: insights from a mathematical model, Cancer Res. 67 (6) (2007) 2729–2735.
[50] M. Wu, H.B. Frieboes, M.A. Chaplain, S.R. McDougall, V. Cristini, J.S. Lowengrub, The effect of interstitial pressure on therapeutic agent transport: coupling with the tumor blood and lymphatic vascular systems, J. Theoret. Biol. 355 (2014) 194–207.
[51] M. de Lucio, M. Bures, A.M. Ardekani, P.P. Vlachos, H. Gomez, Isogeometric analysis of subcutaneous injection of monoclonal antibodies, Comput. Methods Appl. Mech. Engrg. 373 (2021) 113550.
[52] G. Rus, I.H. Faris, J. Torres, A. Callejas, J. Melchor, Why are viscosity and nonlinearity bound to make an impact in clinical elastographic diagnosis? Sensors 20 (8) (2020) 2379.
[53] J. Lopez, M. Ruiz-Toranzo, C. Antich, C. Chocarro-Wrona, E. López-Ruíz, G. Jiménez, J.A. Marchal, Biofabrication of a tri-layered 3D-bioprinted CSC-based malignant melanoma model for personalized cancer treatment, Biofabrication (2022).
[54] J.M. Northcott, I.S. Dean, J.K. Mouw, V.M. Weaver, Feeling stress: The mechanics of cancer progression and aggression, Front. Cell Dev. Biol. 6 (2018) 17.
[55] R.K. Jain, J.D. Martin, T. Stylianopoulos, The role of mechanical forces in tumor growth and therapy, Annu. Rev. Biomed. Eng. 16 (2014) 321–346.
[56] A. Ramírez-Torres, R. Rodríguez-Ramos, J. Merodio, R. Penta, J. Bravo-Castillero, R. Guinovart-Díaz, F.J. Sabina, C. García-Reimbert, I. Sevostianov, A. Conci, The influence of anisotropic growth and geometry on the stress of solid tumors, Internat. J. Engrg. Sci. 119 (2017) 40–49.
[57] F. Montel, M. Delarue, J. Elgeti, D. Vignjevic, G. Cappello, J. Prost, Isotropic stress reduces cell proliferation in tumor spheroids, New J. Phys. 14 (5) (2012) 055008.
[58] J.A. Roper, R.C. Williamson, B. Bally, C.A. Cowell, R. Brooks, P. Stephens, A.J. Harrison, M.D. Bass, Ultrasonic stimulation of mouse skin reverses the healing delays in diabetes and aging by activation of Rac1, J. Invest. Dermatol. 135 (11) (2015) 2842–2851.
[59] W. Lyu, Y. Ma, S. Chen, H. Li, P. Wang, Y. Chen, X. Feng, Flexible ultrasonic patch for accelerating chronic wound healing, Adv. Healthc. Mater. 10 (19) (2021) 2100785.
[60] J.D. Heckman, J.P. Ryaby, J. McCabe, J.J. Frey, R.F. Kilcoyne, Acceleration of tibial fracture-healing by non-invasive, low-intensity pulsed ultrasound, J. Bone Joint Surg. 76 (1) (1994) 26–34.
[61] T.K. Kristiansen, J.P. Ryaby, J. McCABE, J.J. Frey, L.R. Roe, Accelerated healing of distal radial fractures with the use of specific, low-intensity ultrasound. A multicenter, prospective, randomized, double-blind, placebo-controlled study, J. Bone Joint Surg. 79 (7) (1997) 961–973.
[62] M. Arias, J. Campos, J. Soler, Cross-diffusion and traveling waves in porous-media flux-saturated Keller–Segel models, Math. Models Methods Appl. Sci. 28 (11) (2018) 2103–2129.
[63] V.K. Vanag, I.R. Epstein, Cross-diffusion and pattern formation in reaction–diffusion systems, Phys. Chem. Chem. Phys. 11 (6) (2009) 897–912.
[64] Y. Lou, W.-M. Ni, Diffusion, self-diffusion and cross-diffusion, J. Differential Equations 131 (1996) 79–131.
[65] A. Aguirre-Tamaral, M. Cambón, D. Poyato, J. Soler, I. blanco, Predictive model for cytoneme guidance in Hedgehog signaling based on Ihog-Glypicans interaction, Nature Commun. 13 (1) (2022) 1–14.
[66] T. Stylianopoulos, L.L. Munn, R.K. Jain, Reengineering the physical microenvironment of tumors to improve drug delivery and efficacy: from mathematical modeling to bench to bedside, Trends Cancer 4 (4) (2018) 292–319.
[67] M. Glatz, Low frequency shear waves as a potential mechanotherapy approach in cancer, 2019.
[68] M.C. Hoelzl, F. Festy, G. Fruhwirth, R. Sinkus, Impacting cancer cells via mechanical waves: can we change cellular behaviour? in: Proc. Int. Soc. Magn. Reson. Med., 20167, p. 4363.
[69] G. Lorenzo, S.R. Ahmed, D.A. Hormuth II, B. Vaughn, J. Kalpathy-Cramer, L. Solorio, T.E. Yankeelov, H. Gomez, Patient-specific, mechanistic models of tumor growth incorporating artificial intelligence and big data, 2023, arXiv preprint arXiv:2308.14925.